Towards the design of an enriched concrete with enhanced dissipation performances

Daria Scerrato, Ivan Giorgio, Alessandro Della Corte, Angela Madeo, Norman E Dowling, Félix Darve

Towards the design of an enriched concrete with enhanced dissipation performances

D. Scerrato[c], I. Giorgio[a,c,*], A. Della Corte[b], A. Madeo[c,d], N.E. Dowling[c,e,f], F. Darve[c,g]

[a]*Dep. of Structural and Geotechnical Engineering, Università di Roma La Sapienza, 18 Via Eudossiana, Roma, Italy*
[b]*Dep. of Mechanical and Aerospace Engineering, Università di Roma La Sapienza, 18 Via Eudossiana, Roma, Italy*
[c]*MeMoCS International Research Center for the Mathematics & Mechanics of Complex Systems, Università dell'Aquila, Italy*
[d]*Université de Lyon-INSA (Institut National des Sciences Appliquées), Laboratoire de Génie Civil et Ingénierie Environnementale (LGCIE) Bâtiment Coulomb,69100 Villeurbanne, France*
[e]*MSE Department,208 Holden Hall, Mail Stop 0237, Virginia Tech, 445 Old Turner St. Blacksburg, VA, 24061, USA*
[f]*ESM Department,208 Holden Hall, Mail Stop 0237, Virginia Tech, 445 Old Turner St. Blacksburg, VA, 24061, USA*
[g]*Grenoble Institut Polytechnique, Laboratoire Sols Solides Structures Risques, BP 53, 38041 Grenoble cedex 9, France*

The effect of micro-particle addition on internal dissipation of concrete was experimentally investigated. The idea was to increase the internal friction and improve the related damping performances of the material by allowing the presence of micro-particles inside the concrete pores, thus changing the contact interac-tion between internal surfaces of pores. However, a high percentage of micro-particle addition could either hinder the sliding or even degrade the mechanical strength of the material. Thus, the optimal percent-age has to be experimentally determined for every mixtures one considers. In our study, specimens were tested under cyclic loading to evaluate energy dissipation. In some enriched mixtures presenting a not too low water/cement ratio a significant increase in damping capability is observed with respect to standard concrete. We used experimental data to perform a parameter identification and found that the employed micromorphic model is suitable to forecast the dissipative behavior of the material.

1. Introduction

1.1. Concrete and energy dissipation

Concrete is the most common building material, employed since antiquity. However, it still provides examples of very unexpected behaviors, and given its complex nature can be thought as a meta-material, i.e. a material whose macro-scale behavior depends on a complex micro-scale structure, some properties of which can be modified in a controlled manner (see e.g. [1,2]). In this connection, the concept of 'functional structural modifications' is very attractive, according to which properties are designed in order to assume a desired behavior.

The study of dissipation phenomena is of crucial importance for Civil Engineering. The literature potentially useful for the designing of metamaterials in which material particles are endowed with a sort of energy sink, is huge (see e.g. [3–8]). A new micro-structured model for the dissipation in concrete has been presented in [9]. The main purpose of the present paper is to support this model with a much more extended and detailed analysis of the experimental results, and therefore to considerably deepen the amount and the solidity of the experimental evidence there shown.

The fundamental idea is the following: the composite nature of concrete entails the presence of micro-cracks, i.e. internal voids whose length is of about 1–500 μm; they are already present when the concrete has just dried [10–12]. The opposite faces of these micro-cracks, coming in contact in case of suitably large compressive loads (Fig. 1, upper left and right), can have a relative displacement as a consequence of externally induced vibrations, and thus an internal friction force arises, which is responsible for energy dissipation. This physical interpretation of the dissipation, which was supported through the comparison of numerical and experimental data in [9], suggests a natural procedure to improve the dissipative characteristics of the concrete by increasing the internal friction one has to expect between the faces of the micro-cracks. The most simple way to achieve this result is, in fact, the replacement of a small amount of cement powder with a suitable additive — from now on called

* Corresponding author.
E-mail addresses: daria.scerrato@uniroma1.it (D. Scerrato), ivan.giorgio@uniroma1.it (I. Giorgio), alessandro.dellacorte@uniroma1.it (A. Della Corte), angela.madeo@insa-lyon.fr (A. Madeo), ndowling@vt.edu (N. Dowling), felix.darve@3sr-grenoble.fr (F. Darve).

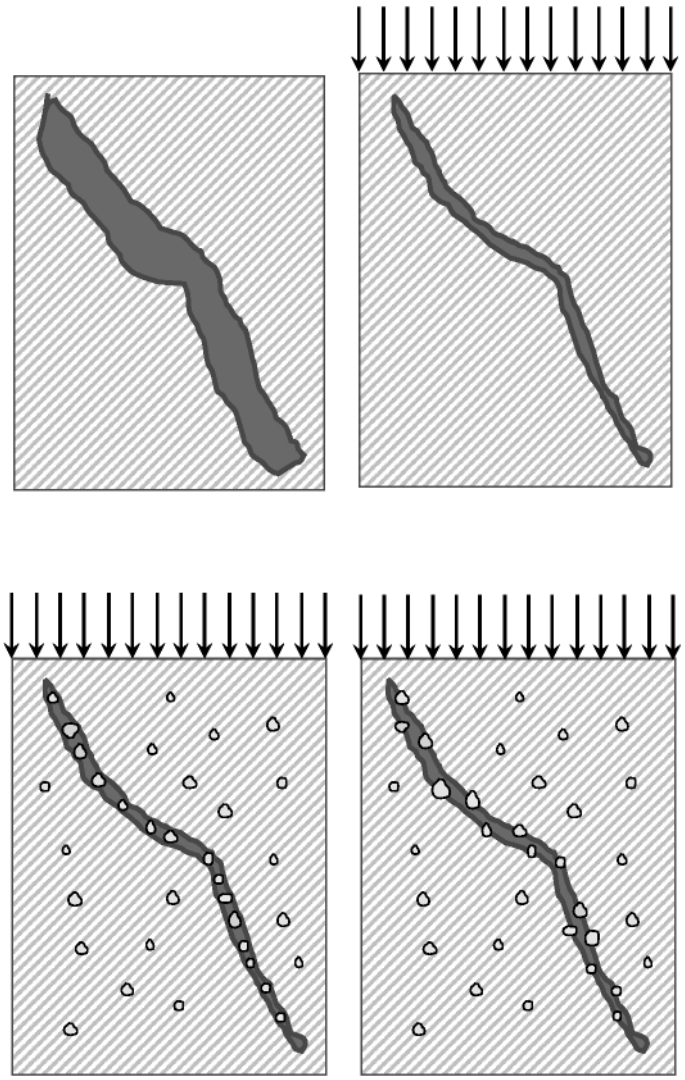

Fig. 1. The reversible mechanism involved in dissipation. Top left: a crack is present as the concrete complete drying. Top right: a load induces contact between the faces; the sliding of the faces due to vibrations causes dissipation. Bottom: a filler has been added to the mixture, replacing a certain amount of cement powder; filler particles inside the cracks (left), or protruding into it from the faces (right) affect dissipation.

'filler' — so as to increase friction. The particles may interact with the sliding of the faces of the cracks in various ways. Indeed, some of them can actually enter into the cracks as they open during the drying process (Fig. 1, bottom left), or they can simply protrude from the crack faces (Fig. 1, bottom right).

The practice of replacing a certain amount of cement powder is rather common and was at first conceived to reduce the cost of the concrete (see e.g. [13,14]) or to chemically improve some properties of the final product. In the experimental work presented in this paper, instead, we employed an admixture which was chemically inactive, and used it to mechanically change the microstructure of the concrete. Of course, one should accurately select the optimal size, hardness, shape and amount of filler to optimize dissipation. In particular, increasing too much the percentage of micro-particle addition can hinder the sliding between the faces of micro-cracks, influencing negatively the dissipation, or even degrade the mechanical strength of the material, and therefore the optimal compromise has to be found between vibration damping and mechanical strength needs. To reach these targets, a suitable experimental campaign had to be designed, practically prepared and executed. The experimental evidence obtained, which will be shown and discussed in the present paper, confirms not only the validity of the model employed for the description of the dissipation, but also supports the abovementioned physical interpretation.

It has to be remarked that we do not claim that the previously described mechanism is responsible for *all* the dissipation. Indeed, dissipation may also arise, as it is well known, from crack opening and formation and other related irreversible modifications. We will come back to this point in Section 3.1. Moreover, we have to remark that a pure viscous model for the internal friction is not suitable for the description of observed phenomena. Indeed, recent measures performed at different frequencies (0.1–0.8 Hz) allowed us to exclude a purely viscous model (see [15]). We therefore selected a mixed Coulomb-viscous model, in which the Coulomb behavior is dominant (see Section 1.2).

The present work lies in a well-established line of investigation concerning concrete manufacturing and enrichment by means of suitable admixtures, but also concerns relevant features regarding mechanical — and more generally physical — properties of the concrete and its micro-structural characterization. Possible applications

of this enhanced concrete can be very relevant and useful, as it has the potential to improve the response of the structures, e.g., to earthquake [16] and wind excitation [17].

The content of the work is organized as follows: in Section 1.2 the theoretical model considered in [9] is recalled and briefly discussed; in Section 2.1, the preparation of the experimental apparatus and some preliminary results are shown; in Section 3, the experimental results in cyclic loading are shown; in Section 4, data are systematically analyzed; finally, in Section 5 the results are discussed, some conclusions are drawn and some possible future lines of investigations are outlined.

1.2. A theoretical model for internal friction in enriched concrete

The model constituting the theoretical basis linked to the experimental work described herein is exposed in [9]. There, in order to write down the Principle of Virtual Work in the framework of a variational formulation (see e.g. [18–20]), a Lagrangian of the following form was considered

$$\mathscr{L} = \mathscr{K} - \Psi = \frac{1}{2}\rho(\dot{\boldsymbol{u}})^2 + \frac{1}{2}\rho_\varphi(\dot{\varphi})^2 - \left(\frac{1}{2}\lambda[\mathrm{tr}(\boldsymbol{E})]^2 + \mu\,\mathrm{tr}(\boldsymbol{E}^2) + \frac{1}{2}k_1\varphi^2 + \frac{1}{3}k_2\varphi^3 + \frac{1}{4}k_3\varphi^4 + \alpha\varphi\sqrt{I_2{}^{(d)}}\right) \tag{1}$$

where λ and μ are the Lamé parameters for linearly elastic isotropic materials, $\boldsymbol{E}$ is the linearized Green–Lagrange strain tensor and the scalar $I_2^{(d)}$ is the second invariant of the deviatoric strain tensor: $I_2{}^{(d)} = \frac{1}{2}\mathrm{tr}(\mathrm{dev}\boldsymbol{E}\,\mathrm{dev}\boldsymbol{E})$, which can be interpreted as a local shear deformation measure. It is worth to remark that the energy density considered can be conceived as a result of a proper homogenization process that can, in principle, originate from a more detailed microstructural model (see e.g. [21–23]). We also observe that in alternative, in order to express the stored energy density of an isotropic material, a pair of elastic constants can be usefully employed: the bulk modulus K and the shear modulus μ (for remarks on the incompressible case see e.g. [24,25]). Finally, the scalar φ is the kinematical descriptor which accounts for the microstructure, and can be interpreted as the average relative displacement of the opposite faces of the micro-cracks. This approach follows the research lines developed for micromorphic continua (see e.g. [26–33]) and can be enhanced to model non-local internal interactions, possibly arising due to the composite nature of concrete, using higher-gradient theories (see e.g. [34–41]). Entering a bit more deeply in the matter, to characterize the influence of interfacial interactions or some effects that can arise from inclusions inside the concrete, the reader is referred to [11,42] and [43,44]. It should also be highlighted that many problems involving dissipation have also been modeled through damage evolution (see e.g. [45–54]), a perspective that can be adopted in other contexts (see e.g. [55–61]). Herein, however, we assume that damage growth is negligible — the load excitation being small enough.

The model 1 has been reduced by means of the standard Saint-Venant theory for simple compression load on cylindrical concrete specimens (see e.g. [62,63]). In its reduced form, it is characterized by two state variables: the deformation parallel to the axis of the cylinder ϵ and the micro-slide φ, and it consists of two equations:

$$\begin{cases} M\ddot{\varepsilon} + K_Y\varepsilon + \tilde{\alpha}\varphi = f_0 + f_1\sin(\omega t) \\ m_\varphi\ddot{\varphi} + \tilde{k}_1\varphi + \tilde{k}_2\varphi^2 + \tilde{k}_3\varphi^3 + \tilde{\alpha}\varepsilon - \tilde{\zeta}\;\varepsilon\;\tanh(\eta\,\dot{\varphi}) = 0 \end{cases} \tag{2}$$

where M and m_φ are respectively an equivalent mass of the concrete sample — i.e. the inertial coefficient acting on ε— and the mass associated to micro-sliding; K_Y is the macro-stiffness, $\tilde{k}_1$, $\tilde{k}_2$, $\tilde{k}_3$ are the elastic parameters which account for deformations of medium microstructure and $\tilde{\alpha}$ is the coupling coefficient between 'micro' and 'macro' structure. The friction force $F = \tilde{\zeta}\,\varepsilon\tanh(\eta\,\dot{\varphi})$ is a generalization of the Coulomb model chosen to match experimental observations and predict the dynamic behavior of concrete. The amplitude of the internal friction is proportional to ε as it is easily seen by representing it as follows

$$\tilde{\zeta}\,\varepsilon = \varpi\mu_k\,\sigma_n = \varpi\mu_k\,K\,(1-2\nu)\,\varepsilon \tag{3}$$

which is the product between the friction coefficient μ_k, the specific surface area ϖ— i.e. the total area of the sliding faces of the micro-cracks per volume unit — and the hydrostatic pressure σ_n— i.e. the compressive stress — which is proportional to the trace $(1-2\nu)\varepsilon$ of the strain tensor and to the bulk modulus K, and is responsible for the closure and the pressing of the pores inside the concrete matrix. The function tanh is introduced to consider a viscous effect in the low velocity range, while the slope η, which represents the inverse of a reference velocity, can be used to modulate the extension of the viscous range. Aiming to describe dissipation in solid continua, as already observed, various approaches have been followed. For instance, either a viscous model of Navier–Stokes-type (see e.g. [49,64–66]) or a model involving internal friction (see e.g. [67–74]) can be taken into account. Our assumption to regularize the function sign of the Coulomb model can be physically interpreted as referred to a hybrid dissipation, in which in a low micro-velocity range the dissipative behavior is primarily viscous, while for high velocities it is essentially Coulomb-type. This regularization, in any case, is useful even from a mathematical and numerical point of view, as the governing ODEs are then of course uniquely solvable and such that periodic forcing terms entail periodic solutions [75].

The complexity of the material and of its behavior requires a numerical formulation especially conceived to avoid common problems, as for instance locking or the so-called hourglass instability; a set of suitable numerical tools are given e.g. in [76–81]. Finally, in experiments of the type here considered, buckling issues may be due to the unavoidable small imperfections in the geometry of the test specimen and in its alignment with respect to the testing machine— for a discussion of the possible tools which may be of use when dealing with this kind of problems, see e.g. [82–87,92,93].

Considering our physical interpretation of dissipation, one can have a rather precise expectation about the qualitative effect of changes in the amount of added filler on dissipation. Indeed, while the presence of 'some' particles inside the micro-cracks can effectively influence the interfacial friction, when the particles are 'too many', it is possible that the deformation of the whole micro-crack is somewhat hindered, which can affect the dissipation capability of the material. Therefore, the addition of a filler can either increase or decrease the friction, and in order to get maximum dissipation one has to find with reasonable precision the optimal amount of filler.

Table 1
Physical and chemical characteristics of GS 4.

Characteristics	Value	Unit
Specific weight	2.71	kg/dm^3
Apparent density	600	g/l
Particles shape	Rhombohedrical	–
White index	80.50	–
Yellow index	3.80	–
Coating power	260	μ
D.O.P. absorption	25.50 ± 1	%
Oil absorption	15.50 ± 1	%
H_2O absorption	18.50 ± 1	%

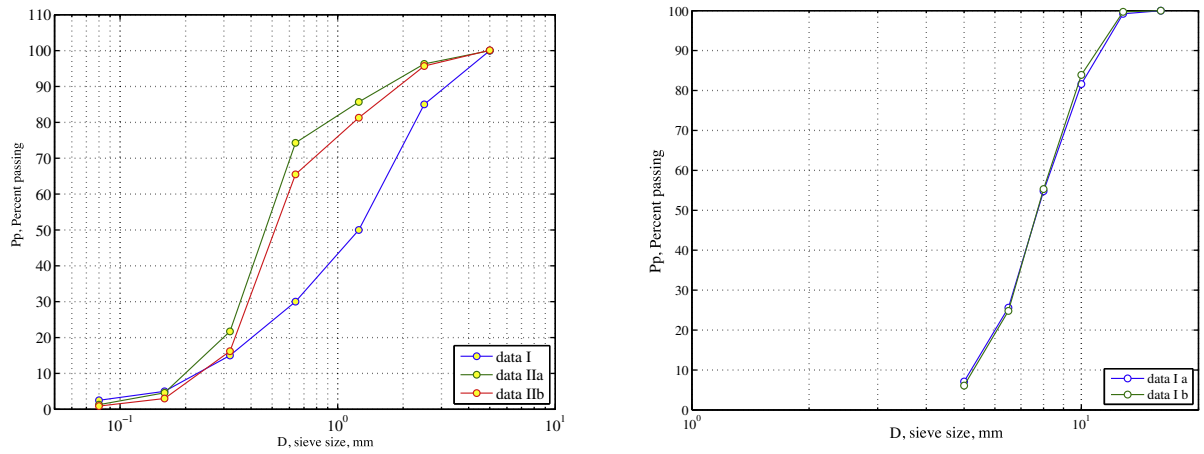

Fig. 2. Granulometric curve of the sand (left) and of the gravel (right) available at the Laboratory LGCIE.

2. Material and methods

2.1. Test specimens and materials

The specimen is a simple cylinder having a ratio of length to diameter, L/d, close to 2. The choice of this ratio represents a compromise. Buckling may occur if L/d ratio is relatively large. If this happens, the test result is not representative of the fundamental compressive behavior of the material. Conversely, if L/d is small, the test result is affected by the details of the conditions at the end. In particular, as the specimen is compressed, the diameter increases due to the Poisson effect, but friction may retard this motion at the ends, resulting in deformation into a barrel shape. This effect can be minimized by a standard capping procedure, entailing proper lubrication of the ends. Thus, the choice of a too small L/d ratio may result in a situation where the behavior of the specimen is dominated by end effects. Considering both the desirability of small L/d to avoid buckling and large L/d to avoid end effects, a reasonable compromise is $L/d \approx 2$ for brittle materials, in which end effects are small. All in all, the chosen test specimens have a circular cross section of diameter $d = 11.28$ cm and a length $L = 22$ cm.

Concrete is a composite material that can be seen as a porous matrix in which pores of two different sizes can be located. In particular, families of pores of almost 10^{-3} μm and of 1–500 μm can be detected. The second ones can be effectively modeled as families of micro-cracks inside an undamaged matrix [52]. These micro-cracks have a great influence on the macroscopic mechanical properties of the concrete since they are expected to determine a decay in the average strength of the material. In order to see how the presence of these additives can affect the friction coefficient between the two faces of each crack, together with the crack density inside the concrete matrix, a series of experimental tests has been prepared. A testing procedure on these new materials has been set up and possible correlations between friction and mechanical properties of concrete have been investigated. It is clear that the friction coefficient depends on the physical properties of the additives, such as the shape and size of the grains and the roughness of the grain surfaces.

The type of additive chosen is GS4; it has such a size (10^0–10^1 μm) to be able to properly interact with micro-cracks, and it also has physical properties which can improve the dynamic behavior of concrete. The main characteristics of this additive are shown in Table 1.

All fillers are obtained from carbonate rocks (such as inert limestone) so that the principal constituent (almost 99%) is Calcium Carbonate ($CaCO_3$). As already said, another parameter that can affect the friction coefficient is the quantity of filler added to the cement powder. It will be shown that the proper amount of replacement can vary depending on the particular mixture one employs. In our case, we selected a 'test' amount of filler on the basis of the research performed in the Virginia Tech Polytechnic Institute (see [88]).

2.2. Specimen preparation

The preparation of samples is one of the most important and sensitive points of our research and it must be conducted carefully.

At the beginning of the test campaign, we analyzed the sand granulometry in order to compute the size distribution of sand grains available at the *Laboratoire de Génie Civil et Ingénierie Environnementale* (LGCIE) of INSA de Lyon. In detail, we performed two granulometric analyses on two samples of dry sand, 1000 g weight each, using standard sieve whose meshes were defined by EN 206-1, 2005. This test allowed us to estimate the rate of each fraction of the sand and to draw the particle size curve. Then these results have been compared with the size distribution of sand grains used in [88], that we considered as our reference curve (see Fig. 2).

Fig. 2 shows the granulometric curve of the sand used in Virginia Tech tests (I) and two curves related to the sand available at Laboratory LGCIE for two different sievings (IIa and IIb). We can note that the fraction of the finest particles (the remainders with grain size lesser than 80 μm) in the case (I) is significantly higher than the other cases (IIa, IIb) — about twice. On the other hand, for the size of retained grains in the range of 160–640 μm the curves IIa and IIb present higher values than the curve I. Concerning the coarsest part of sand, grains greater than 1.25 mm, the percent retained is again higher in the first case rather than in the other two cases. Thus we can observe the different nature of the two sands. Moreover we note that the curves IIa and IIb relative to the two sievings performed are slightly different due to the non-perfect mixture of sand. These analyses on the grain size of sand available in the laboratory LGCIE showed that the differences between the sands were important enough, so we conducted tests on concrete made with

Table 2
Sieve analysis results on sand I.

Sieve size	Percent retained	Cumulative retained %	Percent passing
2.50 mm	15	15	85
1.25 mm	35	50	50
640 μm	20	70	30
320 μm	15	85	15
160 μm	10	95	5
80 μm	2.5	97.5	2.5

Table 3
Sieve analysis results on sand IIa.

Sieve size	Percent retained	Cumulative retained %	Percent passing
2.50 mm	3.7	3.7	96.3
1.25 mm	10.6	14.3	85.7
640 μm	11.4	25.7	74.3
320 μm	52.6	78.3	21.7
160 μm	17.1	95.4	4.6
80 μm	3.3	98.7	1.3

Table 5
Sieve analysis results on gravel Ia.

Sieve size	Percent retained	Cumulative retained %	Percent passing
16.0 mm	0.0	0.0	100
12.8 mm	0.8	0.8	99.2
10.0 mm	17.6	18.4	81.6
8.0 mm	26.8	45.2	54.8
6.5 mm	29.2	74.4	25.6
5.0 mm	18.5	92.9	7.1

both sands. To be able to have significantly comparable results, it was of course worthwhile to reproduce the same sand as in the preceding Virginia Tech tests. Knowing the curve of the desired particle size for the sand, we performed several sieving stages to separate and to stock the different fractions of sand. We repeated this action until the portion of each part was close to the one in the sand required. As a check, we carried out two sieving stages with the same procedure, considering two cases: dry and wet samples. It was noted that the shapes of the granulometric curves, as well as the rate of each fraction, were very close to each other. It was, therefore, concluded that the sand has been recreated with the specifications required by our research. The results of these analyzes are summarized in Tables 2–4.

As for the gravel available to the laboratory LGCIE, a granulometric analysis was performed to obtain data on particle size. Two sievings with the same procedure used in the case of sand (2 samples of dry gravel, whose weight was 1000 g each) were carried out. The size of the particles of gravel could assume less importance than that of sand; the particles of gravel have dimensions much greater than those of sand, as well as those of the filling material. It could be therefore accepted that the gravel does not affect the efficacy of filler. Sieving tests performed on the gravel at laboratory LGCIE were intended to verify the homogeneity of the particle size distribution in order to produce samples with the same physical and mechanical characteristics. The results of the particle size of the gravel are shown in Fig. 2, for two sieving stages (Ia and Ib). The two granulometric curves are very similar, therefore the grain size of the gravel was uniformly distributed, see Tables 5 and 6. To properly assess the amount of water to be used in the concrete mix, the quantity by weight of water contained in the pores of the granular materials used in the mixture was taken into account.

To estimate the amount of water present in the sand and gravel, we adopted the procedure described as follows. We measured the weight of the sample using an accurate balance. The material has then been placed on a plate well heated and we waited a couple of minutes for the excess of water to evaporate. After that, we measured again the weight of the samples in order to estimate the water content by difference. At the end of this procedure, the final volume of gravel and sand present in the mixture was increased in order to compensate for the amount of water filling the voids, and therefore the amount of water added during the preparation of concrete was reduced.

Seven concrete mixtures have been used. All mixtures use differenttypes of Portland cement to produce a 28-day compressive strength of 32 MPa or 52 MPa, a crushed limestones coarse aggregate as shown in Fig. 2, and sand fine aggregate with granulometric curves I and II. Mixtures are characterized by a water-to-cement ratio w_c in the range 0.49–0.69[1] .

Table 4
Sieve analysis results on sand IIb.

Sieve size	Percent retained	Cumulative retained %	Percent passing
2.50 mm	4.4	4.4	95.6
1.25 mm	14.4	18.8	81.2
640 μm	15.8	34.6	65.4
320 μm	49.3	83.9	16.1
160 μm	13.2	97.1	2.9
80 μm	2.1	99.2	0.8

A concrete mix without addition of micro-particles was prepared as a reference material for the sake of comparison. Moreover mixtures with 3% and 3.5% of filler are prepared. We can summarize all the compositions used to make the testing samples, see Tables 7–11. The mixture relative to Tables 7 and 8 is molded with a cement to obtain a grade of concrete of M32 and M52.

In this case, the two strength levels are obtained by using cement powders having different chemical properties, which, when used in the recipe, produce concretes with different nominal strengths.

In Tables 9–11 concrete mixtures are characterized by a compressive strength of 52 MPa, i.e. a grade of concrete M52.

The procedure for the specimen preparation was carried out with care, taking into account the determination of all components. Sand and gravel were inserted in a cement mixer. A part of the quantity of water required was then gradually poured into the mixture thus obtained. After the mixture became sufficiently uniform, the remaining amount of water and the filler, with different percentages depending on the recipe used, were introduced. The filler was added gradually to the mixture, to avoid that the particles being attached to each other. The pouring is continued until achieving of a compound as homogeneous as possible. Regarding the casting of concrete, it was at first filled to one half of the mold. To facilitate the compaction of the mixture and to expel the air, the mold was then placed on a vibrating plate. Finally, we repeated the same procedure until the complete filling of the mold. The specimens thus obtained were subjected to the process of curing in an environment at controlled temperature (≈23°C) for a period of 28 days. The specimens were covered with plastic sheets to avoid excessive drying.

3. Experimental results

3.1. Cyclic tests

Experimental investigations on the dynamic behavior — dissipated energy — of enriched plain concrete have been performed under cyclic uniaxial compressive load. The test machine was controlled to impose a sinusoidal stress with a fixed frequency of $f = 1$ Hz for all the tests. This low frequency was chosen to avoid resonance effects. More particularly, the considered load is

$$\sigma(t) = \left(\frac{\sigma_{\min} + \sigma_{\max}}{2}\right) + \left(\frac{\sigma_{\min} - \sigma_{\max}}{2}\right)\cos(2\pi f\, t)$$

where the values $\sigma_{\min}$, $\sigma_{\max}$ are related to the minimum and maximum forces applied. In detail, we conducted some tests with a force

[1] The w_c ratio (mass ratio of water to cement) is the key factor that determines the strength of concrete. A lower w_c ratio will yield a concrete which is stronger and more durable, while a higher w_c ratio yields a concrete with a larger slump, so it may be placed more easily.

Table 6
Sieve analysis results on gravel Ib.

Sieve size	Percent retained	Cumulative retained %	Percent passing
16.0 mm	0.0	0.0	100
12.8 mm	0.3	0.3	99.7
10.0 mm	15.8	16.1	83.9
8.0 mm	28.6	44.7	55.3
6.5 mm	30.5	75.2	24.8
5.0 mm	18.7	93.9	6.1

ranging from 19.62 to 176.58 kN for the less stiff mixtures, and others with a bigger force between 19.62 and 392.4 kN for the stiffer ones. The peak load was chosen to avoid reaching an unsafe level of stress too close to the compressive strength of concrete material. On the other hand, the minimum level of compressive stress was large enough to ensure interactions of opposite pore surfaces inside the concrete matrix, hence, to enhance the friction of internal contact, on which the dissipated energy depends in the proposed interpretation of the model (1). Opie and Hulsbos [89] reported that repeated or cyclic loading has an adverse effect on concrete strength at stress levels greater than 50% of the compressive strength. For instance, in 5000 cycles of repeated loading, concrete failed at 70% of the ultimate monotonic loading strength. Progressive micro-cracking in the interfacial transition zone and in the matrix is responsible for this phenomenon. Assuming that the stress range applied to the specimen is far enough from the failure stress, however, it can be predicted that an evolution of damage under these conditions due to fatigue phenomenon happens after around one million of cycles [90]. For this reason, a limited number of cycles is considered in all test performed. Specifically, a number of 100 cycles were chosen for each test, which was good enough for a sensible comparison with real seismic activity. In the 100 cycles considered, we observed a practically unchanged relation between σ and ε, which means that no decrease of macroscopic stiffness occurred. Therefore, it can be assumed that the cycling process did not significantly affect the mechanical properties of the specimens. This supports the claim that the observed dissipation is due to reversible mechanism (sliding of the opposite faces of the micro-cracks) described before. A further confirmation of this is provided by Fig. 7, where the (very small) variance of the dissipated energy relative to cycles 50–73 is shown. Further investigation with larger numbers of cycles will be of course of interest to strengthen this result. The strain due to the applied load usually changes as the test progresses. This phenomenon is rapid at first, but the change from one cycle to the next decreases when increasing the number of cycles. The behavior converges towards a conservative limit cycle, and after a small amount of cycles it is already very well approximated by the limit case. The cycles chosen for data analysis are placed after the middle of the experiment — usually the fiftieth cycle — because it is close to the asymptotic behavior of the material.

To be sure that the measured dissipation was not due to friction connected with the testing machine, a cyclic test on an aluminum specimen (alloy 2024-T4) was run. A circular hollow section specimen of external diameter $D = 11.28$ cm, inner diameter $d = 9.5$ cm,

Table 7
Mix I with M32, Mix II with M52: Standard concrete with sand granulometric curve (II), w_c=0.67.

Composition	Weight ratio, kg	Ratio %
Sand	21.25	35.1
Gravel	27.05	46.2
Cement	7.15	12.6
Water	4.8	6.14
Total	35.98	100

Table 8
Mix III with M32, Mix IV with M52: enriched concrete with sand granulometric curve (II) and a use of filler of 3 %, $w_c = 0.69$.

Composition	Weight ratio, kg	Ratio %
Sand	21.25	35.1
Gravel	27.05	46.2
Cement	6.94	11.51
Water	4.8	6.14
Filler	0.2145	0.356
Total	60.25	100

and a length $L = 22$ cm, of precipitation hardened aluminum alloy (see Fig. 4), was tested under the same load range used for the concrete specimens. The aluminum tube has been designed so that the axial strain in concrete specimens is the same as in the aluminum sample, with the load being equal. In formulae:

$$\epsilon_z = \frac{P}{A_{Al}E_{Al}} = \frac{P}{A_cE_c} \Rightarrow \frac{E_{Al}}{E_c} = \frac{A_c}{A_{Al}}$$

where E_{Al} and E_c are respectively the elastic modulus of aluminum and concrete, and A_{Al}, A_c are the areas respectively of the aluminum and concrete specimens.

Assuming the external diameter D to be equal to the concrete specimen diameter, we have

$$\frac{d}{D} = \sqrt{1 - \frac{E_c}{E_{Al}}}.$$

The peak stress induced by this load is approximately equal to 35 MPa which is far below the yield stress of the aluminum (for failure stresses of various aluminum alloys, see Dowling [90]), so that essentially linear-elastic behavior of the system is expected in the absence of internal hysteresis of the machine. A linear elastic behavior was actually measured during the experiments (see Fig. 4), so it can be assumed that the energy dissipation measured from the concrete cyclic test is totally due to friction phenomena inside the specimen. We remark that the dissipation possibly arisen in the contact between the specimen and the machine does not affect the experiment, as we directly measure the deformation of the sample (far enough from end-effects) and the force, which is the same for every cross section of the specimen. As can be seen from Fig. 4, no significant hysteretic behavior can be detected. Since this dissipation is small compared to those measured from concrete specimens, it will be assumed that as equal to zero.

The previous procedure adds soundness to our experimental results con concrete specimens. Anyway, it should be pointed out that, in any case, our experimental apparatus would not have detected any dissipation coming from internal friction of the machine or between the sample and the loading supports. Indeed, the measured deformation is detected by means of strain gauges attached to the central part of the sample, and therefore far from side effects (see Fig. 3), while the force applied in the region equipped with strain gauges is evidently independent from any possible dissipation occurring elsewhere. Therefore, even if a dissipation between the sample and the capping occurs (which is theoretically possible), it would be not appreciated by the experimental apparatus. In other words, the energy dissipation measured from concrete specimens can be totally attributed to real material behavior, rather than to some effects due to the test apparatus.

In earlier tests, we detected the presence of an undesired degree of bending of the concrete specimens due to small misalignment or the lack of complete lateral stability of the actuator, where the latter is due to motion within the restraints of its oil seals. The small lateral instability makes the position of the actuator not precisely defined,

Table 9
MixV: Standard concrete with sand granulometric curve (I), w_c=0.487.

Composition	Weight ratio, kg	Ratio %
Sand	12.5	35.1
Gravel	16.57	46.2
Cement	4.52	12.6
Water	2.39	6.14
Total	35.98	100

so that alignment is not definitive in the application of the compressive load. We examined various methods to reduce the bending, including raising the specimen support by about a meter, improving the alignment, using larger specimens, and finding a suitable off-center location by which the bending is minimized. Finally, to address this issue, we followed a specific procedure to find a suitable off-center location on the basis of the Saint-Venant problem (see for more details [91]). To further validate our physical interpretation of dissipation, it would be interesting to have an estimate of the initial degree of cracking in the different samples, with a particular stress on the effect of the addition of filler. This can be achieved by an accurate measurement of the macroscopic stiffness of the samples, or directly by means of ultra-sonic investigations. Further studies will hopefully be useful in this connection.

3.2. Ramp failure tests

As briefly explained before, each specimen tested under uniaxial cyclic load had finally undergone a ramp test in order to measure its final resistance (Fig. 5). The cylinders are tested on the two planar faces. The compression machine exerts a constant progressing force on the specimens till they fail, the rate of loading is 0.6 ± 0.2 MPa/s (N/mm^2/s). The reading at failure is the maximum compressive strength of the concrete. Table 12 lists the ultimate strength for some representative concrete mixtures. The expected values and the related errors are evaluated from a set of six specimens for each mixture.

As shown in Table 12, a lower water to cement ratio w_c corresponds to a higher level of strength, while a higher w_c entails a larger difference with the nominal value of the strength.

4. Discussion

4.1. Dissipation energy identification

After performing the cyclic tests, stress–strain graphics can be drawn on the basis of the measurements of the force applied to the specimen and deformation acquired by the strain gauges. The area between the upper and the lower curves of a cycle represents the measured energy dissipation of the sample. This energy for each specimen has been measured by means of a precise procedure which will be discussed in the following and the obtained average value (calculated on 6 specimens) is shown in Table 13. The procedure used to measure the energy dissipation can be summarized as follows

1. The mean of the three strain gauge measures $\hat{\epsilon}^{(j)}(t_i)$ with $j = 1, \ldots, 3$ is considered in order to make negligible a little bending effect remaining (see Section 3.1); the stress curve $\hat{\sigma}(t_i)$ is evaluated by dividing the acquired force by the nominal area of the sample.
2. Considering the signals referred to in the previous item of n cycles, the expected value and the variance are estimated splitting the signal in n portions and regarding each cycle as a determination of the corresponding variable. The initial point of the signal is chosen starting from the middle of the experiment — usually the 50th cycle — because from this instant, we can assume reached an asymptotic behavior of the material.
3. The two branches of the loading and unloading curve have been fitted with second order polynomials.
4. The energy dissipation is determined computing the areas under each branches — loading and unloading curve — by means of straightforward calculation (definite integration).

In order to perform the abovementioned procedure, the applied forces and the strain related to the strain gauges are collected as vectors depending on the time. We denote the measured applied external force per unit area by $\hat{\sigma}(t_i)$ at each time t_i of the measure and the deformation acquired by the three strain gauges with $\hat{\epsilon}^{(j)}(t_i)(j = 1, \ldots, 3)$.

Let the set of points (t_i, y_i) be the result from a certain number, n, of determinations of the variable Y as function of the variable time, t, in correspondence of predetermined values of the time t_i. It is assumed that the errors in the values of t_i are negligible compared to those for the values y_i of the variable Y, so we can assume that each t_i is reproduced in repeated measures, while, for each t_i, the y_i fluctuate according to the law of the normal distribution. Under these conditions, for each t_i, it is easy to estimate the parameters of the probability distribution that characterizes a certain dataset $(y_{i1}, \ldots y_{in})$: expected value, μ_i, and variance, s_i^2. For the expected value an effective estimator is the arithmetic mean

$$\overline{Y}_i = \frac{1}{n}\sum_{j=1}^{n} y_{ij} \tag{4}$$

which also has a normal distribution with expected value and variance s_i^2/n. An appropriate estimator for the variance of the sample, however, is given by

$$S_i^2 = \frac{1}{n-1}\sum_{j=1}^{n}\left(y_{ij} - \overline{Y}_i\right)^2. \tag{5}$$

Table 10
Mix VI: Enriched Concrete with sand granulometric curve (I) and a use of filler of 3%, w_c=0.503.

Composition	Weight ratio, kg	Ratio %
Sand	12.5	35.1
Gravel	16.57	46.2
Cement	4.38	12.2
Water	2.39	6.14
Filler	0.13	0.377
Total	35.98	100

Table 11
Mix VII: enriched concrete with sand granulometric curve (I) and a use of filler of 3.5%, w_c=0.507.

Composition	Weight ratio, kg	Ratio %
Sand	12.5	35.1
Gravel	16.57	46.2
Cement	4.36	12.1
Water	2.39	6.14
Filler	0.16	0.439
Total	35.98	100

In order to consider the confidence interval for the expected value μ_i,

it is appropriate to introduce a random variable $\chi_{\mu i}(y_{i1}, y_{i2}, \ldots y_{in})$

$$\chi_{\mu i} = \frac{\bar{Y}_i - \mu_i}{S_i/\sqrt{n}} \tag{6}$$

function of the n sample values $(y_{i1}, y_{i2}, \ldots y_{in})$, to which it is possible to associate the Student's χ-distribution, $f(\chi_{\mu i})$ with $n-1$ degrees of freedom. The knowledge of the statistics of this aleatory variable allows the detection of the probability with which the 'true' value of the parameter μ_i is within a certain range. It is possible to determine, in fact, two parameters $\chi_{1-\alpha/2}$ and $\chi_{\alpha/2}$ such that the integral

$$\int_{\chi_{\alpha/2}}^{\chi_{1-\alpha/2}} f(\chi_{\mu i})\mathrm{d}\chi_{\mu i} = P\left(\chi_{1-\alpha/2} < \chi_{\mu i} < \chi_{\alpha/2}\right) \tag{7}$$

— which represents the probability that the variable $\chi_{\mu i}$ is within the interval $(\chi_{1-\alpha/2}, \quad \chi_{\alpha/2})$ — is equal to a certain value $1-\alpha$, where α is called this level of significance, and is between zero and one. Since the Student's χ-distribution is symmetric with respect to zero from Eq. (7) occurs with probability $1-\alpha$

$$-\chi_{\alpha/2} < \frac{\bar{Y}_i - \mu_i}{S_i/\sqrt{n}} < \chi_{\alpha/2}. \tag{8}$$

The condition for $\chi_{\mu i}$ results for the parameter μ_i in the relationship

$$\bar{Y}_i - \chi_{\alpha/2}\frac{S_i}{\sqrt{n}} < \mu_i < \bar{Y}_i + \chi_{\alpha/2}\frac{S_i}{\sqrt{n}} \tag{9}$$

which allows determining, with probability $1-\alpha$, also called coefficient of confidence, the endpoints of the interval in which falls, within the 'true' value of the parameter μ_i, which by definition is equal to its expected value and is related to the estimation of its average by the relation

$$E[Y] = \bar{Y}_i \pm \chi_{\alpha/2}\frac{S_i}{\sqrt{n}}. \tag{10}$$

Therefore the resulting upper confidence limit E[Y] of the mean can be calculated with 99.5% confidence interval and $n = 24$ degrees of freedom using the following equation

$$E[Y] = \bar{Y}_i \pm 2.797\frac{S_i}{\sqrt{n}} \tag{11}$$

The 99.5% interval indicates that there is a chance of 99.5% that a new observation will fall within the bounds.

Fig. 6 shows, for a representative cycle, the results relative to the items 1 and 2 of the procedure above mentioned, i.e. expected values of the strain ε and the stress σ and an indication of 99.5 % confidence bounds. It is worth noting that the measurement system has a precision[2], related to reproducibility and repeatability, which is very high. The confidence intervals shown in the last figure are evaluated on the basis of the statistical analysis previously performed (see Eq. (11)). Moreover, we can see that the error estimate for the stress has a very low level because the cyclic load is driven by a feedback loop that enhances the precision of the test apparatus. Thus, in what follows we neglect the errors on the stress.

Fig. 7 exhibits the dissipation energy loop with 99.5 % confidence bounds for a typical concrete specimen, represented in a stress–strain plane in which ε and σ are respectively the component of the strain and stress tensors along the cylinder axis projected in the same direction.

Fig. 3. Set up for cyclic test.

The energy dissipation, that is the area between the loading and unloading curves of a cycle, is extracted from the actual measured data by performing polynomial curve fits. To obtain the polynomial coefficient estimates, a least-squares method is employed. The fit was evaluated using the standard R^2 indicator.

4.2. Parameter identification

In this section, we turn our attention to the problem of finding the best material parameter values for the model, in order to interpolate the set of N points $(\sigma_i, \varepsilon_i)$ — i.e., the stress $\sigma_i = \hat{\sigma}(t_i)$ and the mean of the three strain gauge measures $\varepsilon_i =< \hat{\varepsilon}^{(j)}(t_i) >$— resulting from a certain number, n, of measures of these quantities. In this regard, for the regression, we consider the model described in [9]. For the sake of simplicity, we assume that the errors on the values of stress σ_i are much smaller than the errors which affect the values of the strain ε_i, so that it is possible to think that each σ_i attains close results in repeating measurements under unchanged conditions, while for each σ_i, ε values fluctuate, in our assumptions, according to a normal distribution. For each arbitrary value of σ_i the measure of strain ε is represented by the random variable ε_i distributed with expected value $f(\sigma_i; a_1, \ldots a_\nu)$ and variance s_i^2. In particular, the material parameters that we want to estimate are the macro-stiffness K_Y, the micro-stiffnesses $\tilde{k}_1$, $\tilde{k}_2$, $\tilde{k}_3$, the coupling coefficient α and dissipation coefficients $\tilde{\zeta}, \eta$.

Let us set, in the model (2), $\varepsilon_i = f(\sigma_i; a_r)$, where a_r, with r ranging from one to $\nu = 7$, are the parameters to be found. In order to determine the parameters a_r, we choose to minimize the following 'cost' function $\mathscr{C}$

$$\mathscr{C} = \sum_{i=1}^{N} \frac{[\varepsilon_i - f(\sigma_i;\ a_r)]^2}{s_i^2} \tag{12}$$

that is to say: we calculate the minimum of the sum of squared residuals with respect to the expected value $f(\sigma_i; a_r)$ weighted by the

[2] The degree to which repeated measurements under unchanged conditions show the same results.

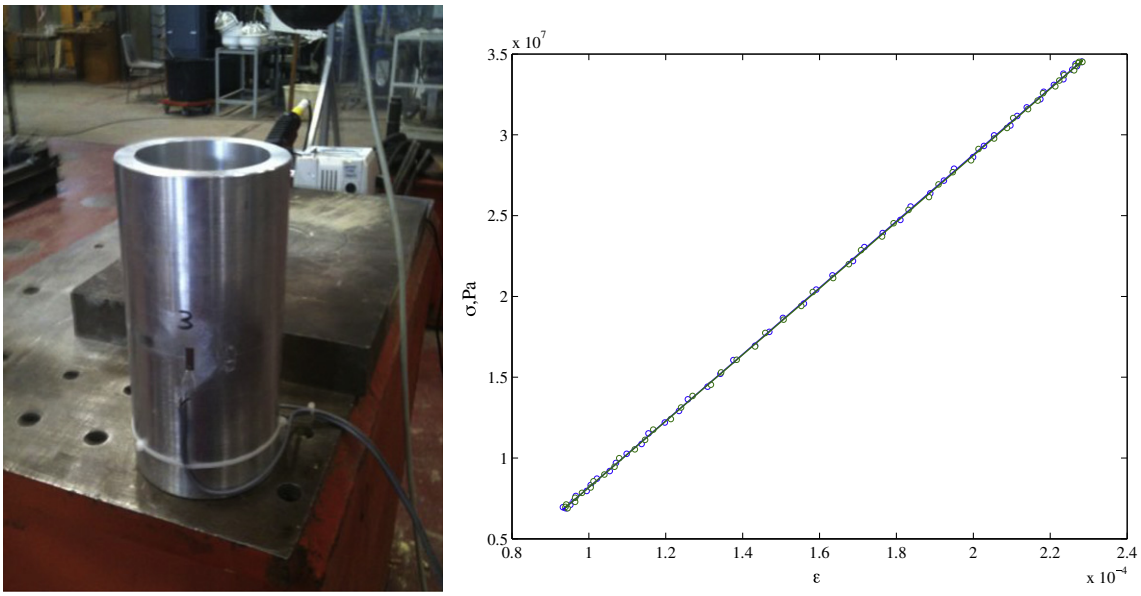

Fig. 4. Measured dissipation loop in aluminum sample.

reciprocal of the variance. In our assumptions we made, the function $\mathscr{C}$ is a χ^2 distribution with $N-\nu$ degrees of freedom.

As a rule of thumb for the χ^2 fitting — remembering that a 'good fit' is achieved when the 2838 chi-square, χ^2/ν, is close to one — we propose that, for the considered number of degrees of freedom (≈ 100), the reduced χ^2 must be less than 1.5.

To avoid further undesirable uncertainties, the input forcing term used in the simulations is the acquired measure of the load in the experimental tests.

Figs. 8–11 exhibit the results of cyclic tests carried out on the specimens, prepared as described above, with mixes I, II, III and IV, respectively (in the graphs, the stress has been renormalized according to the stiffness of the sample). For the sake of comparison, the dissipation loops for a representative cycle are shown in a stress–strain diagram for a standard concrete as a reference material (see Fig. 8) and for a enriched concrete with the addition of 3% of micro-filler (Fig. 9), both for a concrete of strength 32 MPa. Figs. 10 and 11 provide a similar comparison for a concrete with the strength of 52 MPa. It was determined that, up to a certain level, the energy dissipation of the concrete increases with increasing content of micro-particles. On the other hand, as already observed, a further increasing percentage of micro-particle addition can negatively affect the dissipation and even degrade the mechanical strength of material (see thesis [88]). Thus, there is a reasonable compromise in incorporating these micro-particles to obtain higher damping without weakening the mechanical properties.

Fig. 5. A ramp test to measure compressive strength.

Table 12
Nominal and measured strength for the concrete mixtures examined (evaluated on a set of six specimens).

Mix	Type	w_c	Grade of Concrete	Ultimate Strength
I	Standard	0.67	M32	24.8 ± 2.5 MPa
II	Standard	0.67	M52	40.0 ± 4.0 MPa
III	GS4 3%	0.69	M32	20.3 ± 2.0 MPa
IV	GS4 3%	0.69	M52	30.9 ± 3.1 MPa
V	Standard	0.487	M52	51.0 ± 5.1 MPa
VI	GS4 3%	0.503	M52	51.3 ± 5.2 MPa
VII	GS4 3.5%	0.507	M52	59.0 ± 5.8 MPa

Table 13
Dissipated energy for the concrete mixtures examined (evaluated on a set of six specimens).

Mix	Type	Grade of concrete	Dissipated energy per cycle
I	Standard	M32	0.891 ± 0.067 J
II	Standard	M52	0.167 ± 0.014 J
III	GS4 3%	M32	1.31 ± 0.098 J
IV	GS4 3%	M52	0.368 ± 0.027 J
V	Standard	M52	0.824 ± 0.061 J
VI	GS4 3%	M52	0.729 ± 0.056 J
VII	GS4 3.5%	M52	0.364 ± 0.028 J

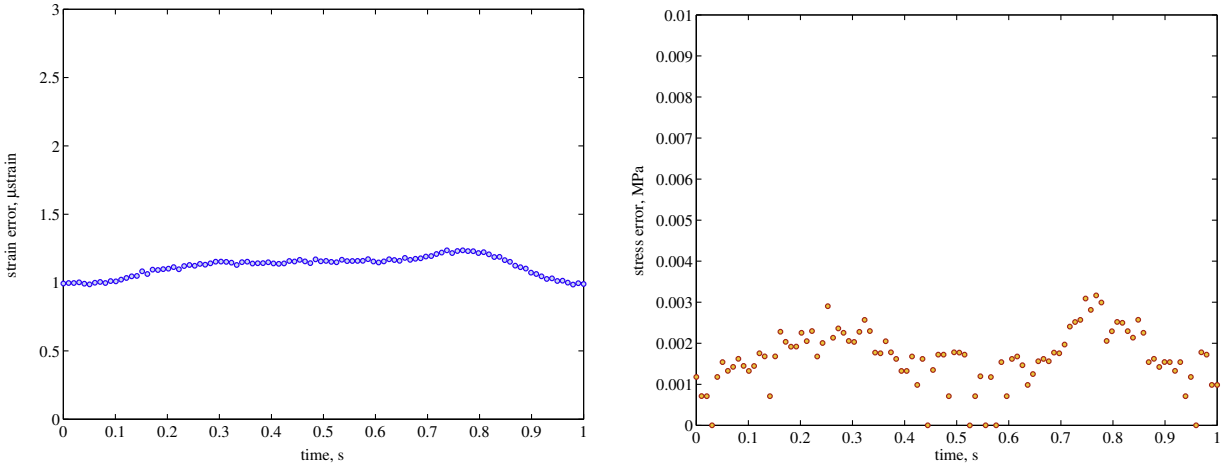

Fig. 6. Error estimates of the strain ε and the stress σ.

It is worth noting that the mixtures with strength of 32 MPa exhibit a more significant dissipative effect than the mixtures with strength of 52 MPa with the considered amount of filler. In fact, the latter types of samples are more rigid, and therefore the micro-relative displacements of pore's faces inside the concrete matrix are smaller. Comparing the two pictures of Figs. 8 and 9 for a M32 grade of concrete, it is possible to notice an increase of a cycle deformation magnitude from about 650 µstrain to 750 µstrain passing from the mix I, i.e. a standard concrete, to the mix III, that is an enriched concrete with a 3% of filler. Analogously, the Figs. 10 and 11 for a M52 grade of concrete, it is possible to note an increase of a cycle deformation magnitude from about 530 µstrain to 600 µstrain passing from the mix II, i.e. a standard concrete, to the mix IV, that is a enriched concrete with a 3% of filler. Given this results, it is clear that the improvement in total dissipation is also due on the increased friction surface in the same loading conditions. Anyway, it should be pointed out that this contribution is not a major one, since adding the filler increases the total dissipation by a ratio of approximately 1.5 (mixtures III vs. I) or 2 (mixtures IV vs. II), whereas the elongation only increases by about 10%. Therefore, one must conclude that the most of improvement in dissipation is not due just to the increased friction surface.

In Table 13, the dissipation energy measured for the seven concrete mixtures are listed. The expected values and the related errors are evaluated from a set of six specimens for each mixture with a cyclic load at a frequency of 1 Hz.

In Table 14, material parameters estimated by curve fitting are listed for the mixes I and II (the label 'St M32' and 'St M52' standing for a M32 and M52 grade of standard concrete, respectively) and the mixes III and IV (the label '$GS4_3$ M32' and '$GS4_3$M52' standing for a M32 and M52 grade of enriched concrete with 3% replacement of micro-filler, respectively).

As already observed, one cannot expect in advance that the optimal amount of filler is the same for all the possible concrete mixtures. Indeed, lower dissipation values for enriched concrete are seen in Fig. 12 show dissipation loops for each of mixes V, VI and VII with M52 grade of concrete and a content of filler increasing: 0%, 3%, and 3.5% (as before, the stress has been renormalized according to the stiffness of the sample). In this case, according to our interpretation, the amount of filler is such that the porosity of the concrete — or the motility of the microcracks faces — is reduced, and therefore the capability of relative displacement between the opposite pore faces is decreased, which in turn implies a smaller dissipation.

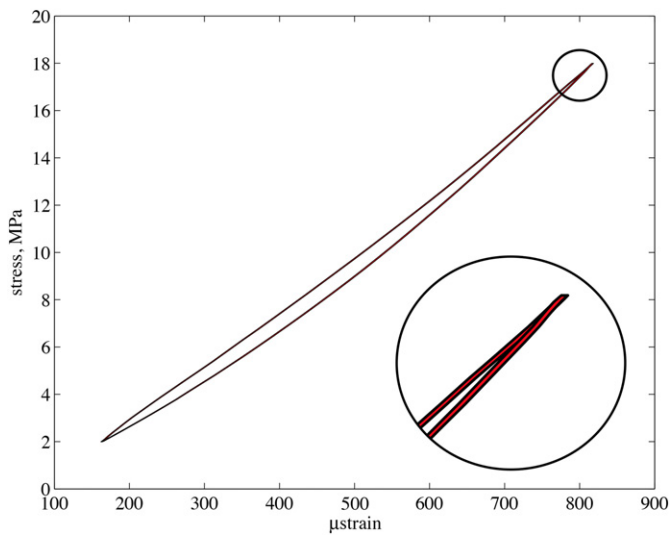

Fig. 7. Dissipation loop (confidence bounds are appreciable in the zoom).

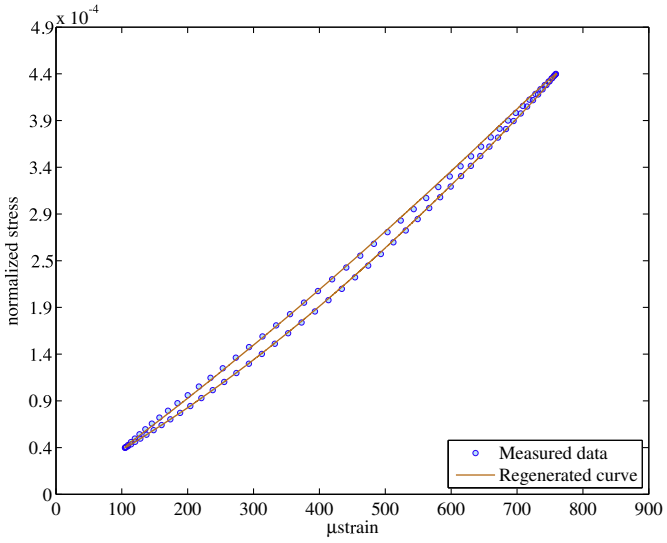

Fig. 8. Mix I: dissipation loop for a M32 grade of standard concrete.

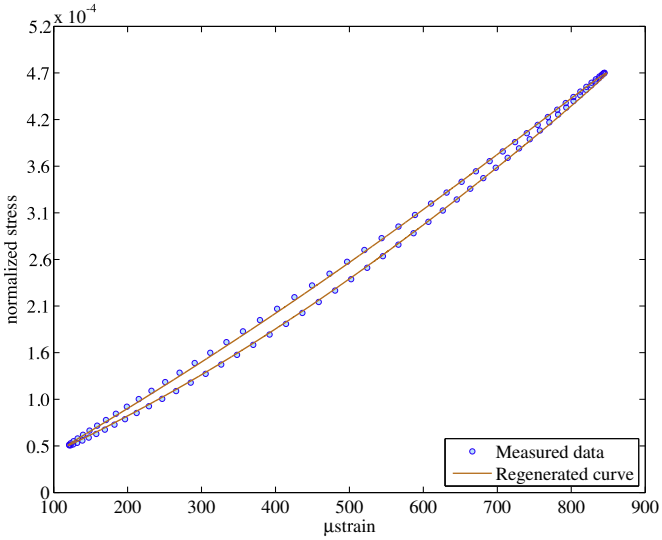

Fig. 9. Mix III: dissipation loop for a M32 grade of enriched concrete.

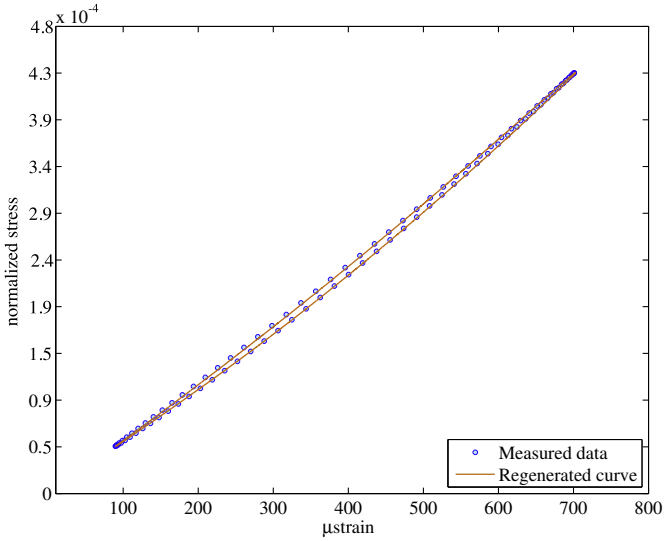

Fig. 11. Mix IV: dissipation loop for a M52 grade of enriched concrete.

A further analysis that can be performed concerns the relationship between the effect of the addition of filler respectively on dissipation properties and on the stiffness of the sample. In Fig. 13 we plotted on the vertical axis the differences (among standard and enriched concrete) in the minimum length reached by the sample during the cycle; since the load is the same in all cases, this magnitude can reasonably account for the stiffness. On the horizontal axis, we plotted the corresponding differences in total dissipated energy. Specifically, the data are relative to a comparison between the mixtures indicated next to the plotted values (roman numbers refer to Table 13). As one can see, sharply and moderately hindered dissipation correspond respectively to sharply and moderately increased stiffness; when instead the dissipation is improved by the addition of the filler, the stiffness results decreased independently of the amount of dissipation.

These results (though admittedly based on a small set of data) is consistent with the proposed interpretation of the dissipation.

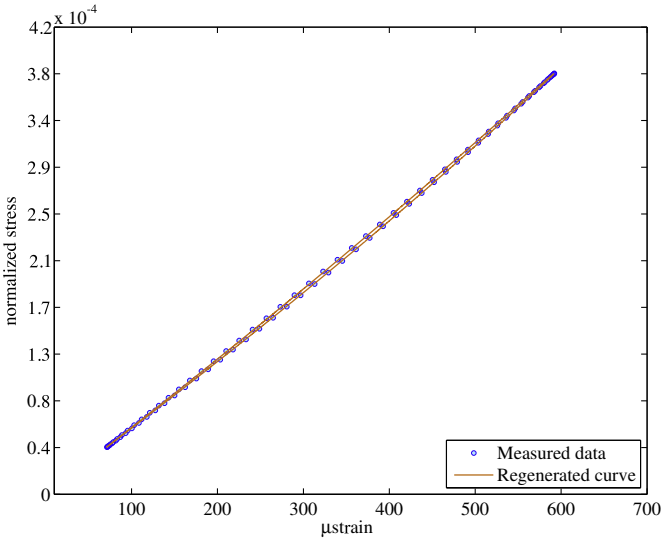

Fig. 10. Mix II: dissipation loop for a M52 grade of standard concrete.

Indeed, according to it, a decreased dissipation is due to the fact that the particles present inside the micro-cracks are in average too numerous to allow proper sliding of the opposite faces; this implies that a certain number of micro-cracks, which where empty before adding the filler, are filled by it, thus resulting in an increased global stiffness, and that this effect should increase as the dissipation decreases (as observed). On the other hand, when the dissipation is improved by the addition of the filler, it means in our interpretation that the particles are in such a number as not to hinder the sliding of the faces, and therefore the micro-cracks that were empty before the addition of the filler are still more or less so. The resulting effect on the stiffness is then due to the particles present as inclusions in the bulk rather than the ones inside the micro-cracks, and should be therefore independent of the dissipation behavior (again as observed).

In Table 15, material parameters estimated by curve fitting are listed for the mix V (the label 'St M52' standing for a M52 grade of standard concrete), the mix VI (the label '$GS4_3$ M52' standing for a M52 grade of enriched concrete with 3% replacement of micro-filler), and the mix VII (the label '$GS4_{3.5}$ M52' standing for a M52 grade of enriched concrete with 3.5% replacement of micro-filler).

5. Conclusions

As our experimental tests and our statistical analysis show, the model (2) is able to reasonably forecast the behavior of the observed phenomena. Indeed, the measured data for dissipation, when compared to theoretical previsions, present a good statistical fit.

Parameter estimation plays of course a critical role in accurately describing the behavior of the system by means of mathematical models. Thus, a figure of merit is required to understand how

Table 14
Material parameters of mixes I, II, III and IV.

Symbol	Fit I (St M32)	Fit III ($GS4_3$ M32)	Fit II (St M52)	Fit IV ($GS4_3$ M52)	Unit
K_Y	8.93×10^7	8.40×10^7	1.04×10^8	9.10×10^7	Nm
$\tilde{k}_1$	4.09×10^9	4.09×10^9	4.62×10^9	4.62×10^9	N/m
$\tilde{k}_2$	2.07×10^{11}	2.07×10^{11}	2.07×10^{11}	2.64×10^{11}	N/m^2
$\tilde{k}_3$	2.68×10^{17}	1.98×10^{17}	2.20×10^{17}	3.08×10^{17}	N/m^3
$\tilde{\alpha}$	4.40×10^8	4.38×10^8	4.40×10^8	4.40×10^8	N
$\tilde{\zeta}$	7.26×10^8	5.50×10^8	1.76×10^8	4.62×10^8	N
η	2.00×10^2	2.00×10^2	2.00×10^2	2.00×10^2	s/m

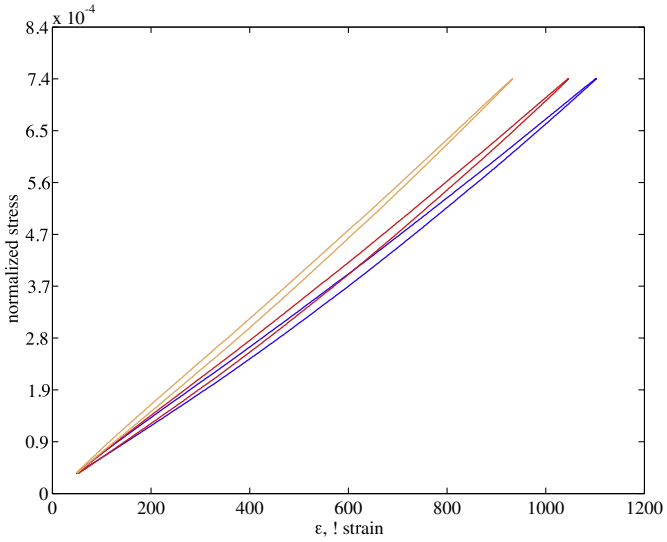

Fig. 12. The dissipation loops for the first three mixtures considered. From right to left: mix V (standard concrete), mix VI (enriched concrete with 3% of micro-filler) and mix VII (enriched concrete with 3.5% of micro-filler).

good is the identification we made. By means of a suitable parameters identification, one can indeed identify the changes involved when the micro-filler is added in a certain percentage, and check to which extent the theoretical previsions are able to capture the phenomenon. Herein, the parameter identification performed by the method presented in Section 4.2, has been validated by the χ^2 test to assess the goodness of the fit.

This analysis showed that, in the examined cases, there are concrete mixtures for which the proposed model is directly acceptable, and cases in which the value of the reduced χ^2 is higher than the minimum threshold chosen for the test.

The mixtures of concrete with a high reduced χ^2 are:

- Mix VII with 3.5% replacement of micro-filler and a compressive strength of 52 MPa;
- Mix I with standard concrete and a compressive strength of 32 MPa;

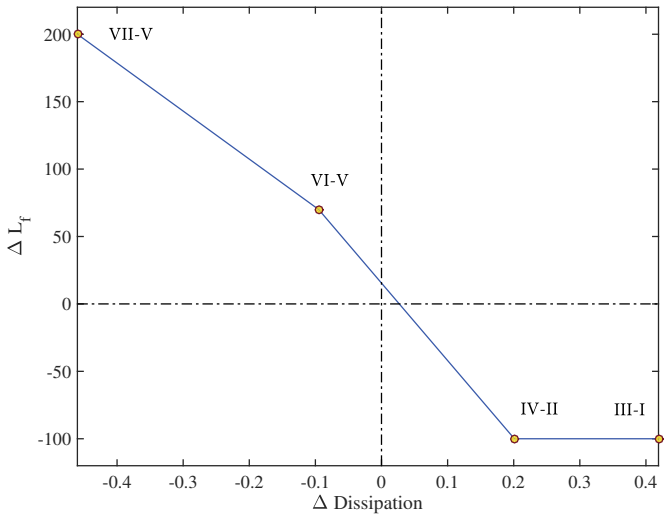

Fig. 13. Differences among standard and enriched concrete in the minimum length of the sample (vertical axis) vs. the corresponding differences in total dissipated energy (roman numbers refer to Table 13).

- Mix II with standard concrete and a compressive strength of 52 MPa.

For these cases, further experimental work is probably needed to achieve the same degree of statistical reliability we obtained in the other cases.

The identifications performed allow us to characterize the effect of each material parameter introduced in the proposed model. Indeed, when the water-to-cement ratio is higher ($w_c \simeq 0.7$), as for mixes I, II, III and IV, the coupling coefficient $\tilde{\alpha}$ seems not to be affected by the micro-particle content (see Table 14). On the contrary, from Table 15 concerning mixes V, VI and VII, it is possible to note that the coupling coefficient $\tilde{\alpha}$ decreases when increasing the content of filler, i.e. the effect of the micro-slip is decreased by adding more filler for mixtures that have a low water-to-cement ratio w_c ($w_c \simeq 0.5$). Recalling our interpretation of the considered dissipative phenomena, this suggests that we are already beyond the optimal percentage of replacement.

In mixes I, II, III and IV, the friction coefficient $\tilde{\zeta}$ appears to be related to the non-linearity of the micro-structure; in fact, considering the micro-stiffness ratios $\tilde{k}_3/\tilde{k}_1$ and $\tilde{k}_2/\tilde{k}_1$, which are measures of nonlinearity, it is possible to note that the greater the ratios, the higher is the friction coefficient $\tilde{\zeta}$. The ratio $\tilde{k}_3/\tilde{k}_1$ is respectively equal to 6.56×10^7, 4.76×10^7, 4.84×10^7 and 6.67×10^7, in the same way the ratio $\tilde{k}_2/\tilde{k}_1$ is 50.5, 44.8, 50.5 and 57.1 and the coefficient $\tilde{\zeta}$ equals 3.3×10^{11} N, 8.0×10^{10} N, 2.50×10^{11} N and, 2.10×10^{11}. The same relationship can be found in the cases of mixes V, VI and VII, In fact, for these last mixtures the ratio $\tilde{k}_3/\tilde{k}_1$ is equal to 5.59×10^7, 8.06×10^6 and 2.82×10^7, respectively and the coefficient $\tilde{\zeta}$ equals 7.4×10^{10} N, 2.43×10^{10} N and 5.31×10^{10} N. In these cases the ratio $\tilde{k}_2/\tilde{k}_1$, is less relevant because the very low values of $\tilde{k}_2$.

Furthermore, including in the model proposed both Coulomb and viscous effects — such that the viscous dissipation is dominant in the low micro-slip velocity range while Coulomb friction is significant beyond a given micro-velocity level — the dissipation slope η plays a crucial role in defining the extension of the ranges corresponding to these different behaviors. For mixes V, VI and VII, when the water-to-cement ratio is low ($w_c \simeq 0.5$), the dissipation slope η is one order of magnitude greater than that of the other mixtures which are characterize by a greater w_c; hence, these three mixtures show a more considerable Coulomb effect.

Let us, finally, draw some conclusions on the work we did. As our data in Table 13 showed, we verified that adding the micro-filler does change the dissipative behavior of the material in a significant way. In our physical interpretation, one has to expect the existence of an 'optimal' value for the amount of added filler in order to obtain maximum dissipation. In two cases, the addition of a 3% of filler markedly enhanced dissipation. Indeed, enriched mixtures II and IV compared to standard mixtures I and III show a significant increase in the total dissipated energy per cycle, with a ratio of about 1.5 and 2, respectively, when compared with the standard case. When dealing with a stiffer mixture, one still observes a significant effect of the addition of the filler on the dissipation, but the measured data suggest that the considered amount of replacement (3–3.5%) is not optimal, and

Table 15
Material parameters of mixes V, VI and VII.

Symbol	Fit V (St M52)	Fit VI ($GS4_3$ M52)	Fit VII ($GS4_{3.5}$ M52)	Unit
K_Y	1.06×10^8	1.28×10^8	1.20×10^8	Nm
$\tilde{k}_1$	4.24×10^9	2.12×10^9	2.12×10^9	N/m
$\tilde{k}_2$	1.76×10^5	2.64×10^5	2.64×10^5	N/m^2
$\tilde{k}_3$	2.37×10^{17}	1.71×10^{16}	5.98×10^{16}	N/m^3
$\tilde{\alpha}$	3.96×10^8	3.30×10^8	2.59×10^8	N
$\tilde{\zeta}$	1.63×10^8	5.34×10^7	1.17×10^8	N
η	9.85×10^3	7.88×10^3	7.88×10^3	s/m

that tests with a lower replacement percentage are required to identify the optimal value. On the whole, the theoretical previsions are consistent with the observed data, and further experimental studies are needed to determine the optimal amount of filler in a wider class of mixtures. Of course, the possibility to further develop the model in order to theoretically forecast the optimal amount of filler is still an open and very interesting scientific challenge.

References

[1] D. Del Vescovo, I. Giorgio, Dynamic problems for metamaterials: review of existing models and ideas for further research, Int. J. Eng. Sci. 80 (2014) 153–172.

[2] A. Madeo, L. Placidi, G. Rosi, Towards the design of metamaterials with enhanced damage sensitivity: second gradient porous materials, Res. Nondestruct. Eval. 25 (2) (2014) 99–124.

[3] A. Carcaterra, A. Akay, Theoretical foundations of apparent-damping phenomena and nearly irreversible energy exchange in linear conservative systems, J. Acoust. Soc. Am. 121 (4) (2007) 1971–1982.

[4] A. Carcaterra, A. Akay, Dissipation in a finite-size bath, Phys. Rev. E 84 (1) (2011) 011121.

[5] N. Roveri, A. Carcaterra, A. Akay, Energy equipartition and frequency distribution in complex attachments, J. Acoust. Soc. Am. 126 (1) (2009) 122–128.

[6] S. Vidoli, F. dell'Isola, Vibration control in plates by uniformly distributed PZT actuators interconnected via electric networks, Eur. J. Mech. A. Solids 20 (3) (2001) 435–456.

[7] S. Vidoli, F. dell'Isola, Modal coupling in one-dimensional electromechanical structured continua, Acta Mech. 141 (1-2) (2000) 37–50.

[8] M. Porfiri, F. dell'Isola, E. Santini, Modeling and design of passive electric networks interconnecting piezoelectric transducers for distributed vibration control, Int. J. Appl. Electromagn. Mech. 21 (2) (2005) 69–87.

[9] D. Scerrato, I. Giorgio, A. Madeo, A. Limam, F. Darve, A simple non-linear model for internal friction in modified concrete, Int. J. Eng. Sci. 80 (2014) 136–152.

[10] P.K. Mehta, P.J.M. Monteiro, Concrete: Microstructure, Properties, and Materials, vol. 3. McGraw-Hill, New York, 2006.

[11] H.S. Wong, M. Zobel, N.R. Buenfeld, R.W. Zimmerman, Influence of the interfacial transition zone and microcracking on the diffusivity, permeability and sorptivity of cement-based materials after drying, Mag. Concr. Res. 61 (8) (2009) 571–589.

[12] P. Grassl, H.S. Wong, N.R. Buenfeld, Influence of aggregate size and volume fraction on shrinkage induced micro-cracking of concrete and mortar, Cem. Concr. Res. 40 (1) (2010) 85–93.

[13] A. Misra, D. Biswas, S. Upadhyaya, Physico-mechanical behavior of self-cementing class C fly ash-clay mixtures, Fuel 84 (11) (2005) 1410–1422.

[14] K.M.A. Hossain, M. Lachemi, Strength, durability and micro-structural aspects of high performance volcanic ash concrete, Cem. Concr. Res. 37 (5) (2007) 759–766.

[15] I. Giorgio, D. Scerrato, Multi-scale concrete model with rate-dependent internal friction, Eur. J. Environ. Civ. Eng. (2016) http://dx.doi.org/10.1080/19648189.2016.1144539.

[16] S.S. Bhattacharjee, P. Leger, Seismic cracking and energy dissipation in concrete gravity dams, Earthq. Eng. Struct. Dyn. 22 (11) (1993) 991–1007.

[17] L. Pagnini, Reliability analysis of wind-excited structures, J. Wind Eng. Ind. Aerodyn. 98 (1) (2010) 1–9.

[18] L. Placidi, F. dell'Isola, N. Ianiro, G. Sciarra, Variational formulation of pre-stressed solid-fluid mixture theory, with an application to wave phenomena, Eur. J. Mech. A. Solids 27 (4) (2008) 582–606.

[19] F. dell'Isola, M. Guarascio, K. Hutter, A variational approach for the deformation of a saturated porous solid. A second-gradient theory extending Terzaghi's effective stress principle, Arch. Appl. Mech. 70 (5) (2000) 323–337.

[20] A. Madeo, F. dell'Isola, P. Seppecher, Boundary conditions at fluid-permeable interfaces in porous media: a variational approach, Int. J. Solids Struct. 46 (17) (2009) 3150–3164.

[21] L. Dormieux, D. Kondo, F-J. Ulm, Strength Homogenization, Microporomechanics, John Wiley & Sons 2006,

[22] N. Auffray, R. Bouchet, Y. Brechet, Strain gradient elastic homogenization of bidimensional cellular media, Int. J. Solids Struct. 47 (13) (2010) 1698–1710.

[23] A. Misra, Y. Yang, Micromechanical model for cohesive materials based upon pseudo-granular structure, Int. J. Solids Struct. 47 (21) (2010) 2970–2981.

[24] S. Federico, A. Grillo, G. Wittum, Considerations on incompressibility in linear elasticity, Il Nuovo Cimento Soc. Ital. Fis., C 32 (1) (2009) 81.

[25] S. Federico, A. Grillo, S. Imatani, The linear elasticity tensor of incompressible materials, Math. Mech. Solids 20 (6) (2014) 643–662.

[26] A.C. Eringen, Microcontinuum Field Theories., Springer 1999.

[27] S. Forest, R. Sievert, Nonlinear microstrain theories, Int. J. Solids Struct. 43 (24) (2006) 7224–7245.

[28] W. Pietraszkiewicz, V.A. Eremeyev, On vectorially parameterized natural strain measures of the non-linear Cosserat continuum, Int. J. Solids Struct. 46 (11) (2009) 2477–2480.

[29] P. Neff, I-D. Ghiba, A. Madeo, L. Placidi, G. Rosi, A unifying perspective: the relaxed linear micromorphic continuum, Contin. Mech. Thermodyn. 26 (5) (2014) 639–681.

[30] P. Neff, J. Lankeit, A. Madeo, On Grioli's minimum property and its relation to Cauchy's polar decomposition, Int. J. Eng. Sci. 80 (2014) 209–217.

[31] S. Federico, W. Herzog, On the permeability of fibre-reinforced porous materials, Int. J. Solids Struct. 45 (7) (2008) 2160–2172.

[32] M. Ferretti, A. Madeo, F. dell'Isola, P. Boisse, Modeling the onset of shear boundary layers in fibrous composite reinforcements by second-gradient theory, Z. Angew. Math. Phys. 65 (3) (2014) 587–612.

[33] B. Nadler, P. Papadopoulos, D.J. Steigmann, Multiscale constitutive modeling and numerical simulation of fabric material, Int. J. Solids Struct. 43 (2) (2006) 206–221.

[34] P. Kotronis, R. Chambon, J. Mazars, F. Collin, Local second gradient models and damage mechanics: application to concrete, 11th International Conference on Fracture, Turin, Italy, Org. ICF, cd, paper, Vol. 5712, 2005. pp. 20–25.

[35] A. Madeo, F. dell'Isola, F. Darve, A continuum model for deformable, second gradient porous media partially saturated with compressible fluids, J. Mech. Phys. Solids 61 (11) (2013) 2196–2211.

[36] F. dell'Isola, U. Andreaus, L. Placidi, At the origins and in the vanguard of peridynamics, non-local and higher-gradient continuum mechanics: an underestimated and still topical contribution of Gabrio Piola, Math. Mech. Solids 20 (8) (2015) 887–928. http://dx.doi.org/10.1177/1081286513509811.

[37] J-J. Alibert, P. Seppecher, F. dell'Isola, Truss modular beams with deformation energy depending on higher displacement gradients, Math. Mech. Solids 8 (1) (2003) 51–73.

[38] G. Sciarra, F. dell'Isola, O. Coussy, Second gradient poromechanics, Int. J. Solids Struct. 44 (20) (2007) 6607–6629.

[39] Y. Yang, W.Y. Ching, A. Misra, Higher-order continuum theory applied to fracture simulation of nanoscale intergranular glassy film, J. Nanomech. Micromech. 1 (2) (2011) 60–71.

[40] Y. Yang, A. Misra, Higher-order stress-strain theory for damage modeling implemented in an element-free Galerkin formulation, Comput. Model. Eng. Sci. 64 (1) (2010) 1–36.

[41] F. dell'Isola, P. Seppecher, A. Madeo, How contact interactions may depend on the shape of Cauchy cuts in Nth gradient continua: approach "à la D'Alembert", ZAMP - Zeitschrift für Angewandte Mathematik und Physik / Journal of Applied Mathematics and Physics 63 (6) (2012) 1119–1141.

[42] F. dell'Isola, A. Romano, On the derivation of thermomechanical balance equations for continuous systems with a nonmaterial interface, Int. J. Eng. Sci. 25 (11) (1987) 1459–1468.

[43] F. dell'Isola, L. Rosa, C. Woźniak, Dynamics of solids with microperiodic nonconnected fluid inclusions, Arch. Appl. Mech. 67 (1997) 215–228.

[44] F. dell'Isola, L. Rosa, C. Woźniak, A micro-structured continuum modelling compacting fluid-saturated grounds: the effects of pore-size scale parameter, Acta Mech. 127 (1-4) (1998) 165–182.

[45] L. Adelaide, B. Richard, F. Ragueneau, C. Cremona, Thermodynamical admissibility of a set of constitutive equations coupling elasticity, isotropic damage and internal sliding, C.R. Mec. 338 (3) (2010) 158–163.

[46] Z. Boukria, A. Limam, Experimental damage analysis of concrete structures using the vibration signature-Part II: located damage (crack), Int. J. Mech. 6 (1) (2012) 28–34.

[47] F. Bourgeois, N. Burlion, J-F. Shao, Modelling of elastoplastic damage in concrete due to desiccation shrinkage, Int. J. Numer. Anal. Methods Geomech. 26 (8) (2002) 759–774.

[48] F. D'Annibale, A. Luongo, A damage constitutive model for sliding friction coupled to wear, Contin. Mech. Thermodyn. 25 (2-4) (2013) 503–522.

[49] A. Misra, V. Singh, Micromechanical model for viscoelastic materials undergoing damage, Contin. Mech. Thermodyn. 25 (2-4) (2013) 343–358.

[50] G.D. Nguyen, G.T. Houlsby, A coupled damage-plasticity model for concrete based on thermodynamic principles: Part I: model formulation and parameter identification, Int. J. Numer. Anal. Methods Geomech. 32 (4) (2008) 353–389.

[51] G.D. Nguyen, G.T. Houlsby, A coupled damage-plasticity model for concrete based on thermodynamic principles: Part II: non-local regularization and numerical implementation, Int. J. Numer. Anal. Methods Geomech. 32 (4) (2008) 391–413.

[52] V. Pensée, D. Kondo, L. Dormieux, Micromechanical analysis of anisotropic damage in brittle materials, J. Eng. Mech. 128 (8) (2002) 889–897.

[53] G. Pijaudier-Cabot, K. Haidar, J-F. Dubé, Non-local damage model with evolving internal length, Int. J. Numer. Anal. Methods Geomech. 28 (7-8) (2004) 633–652.

[54] A. Rinaldi, L. Placidi, A microscale second gradient approximation of the damage parameter of quasi-brittle heterogeneous lattices, Z. Angew. Math. Phys. 94 (10) (2014) 862–877.

[55] L. Placidi, S.H. Faria, K. Hutter, On the role of grain growth, recrystallization and polygonization in a continuum theory for anisotropic ice sheets, Ann. Glaciol. 39 (1) (2004) 49–52.

[56] U. Andreaus, P. Baragatti, Fatigue crack growth, free vibrations, and breathing crack detection of aluminium alloy and steel beams, J. Strain Anal. Eng. Des. 44 (7) (2009) 595–608.

[57] T. Lekszycki, F. dell'Isola, A mixture model with evolving mass densities for describing synthesis and resorption phenomena in bones reconstructed with bio-resorbable materials, Z. Angew. Math. Mech. 92 (6) (2012) 426–444.

[58] A. Madeo, D. George, T. Lekszycki, M. Nierenberger, Y. Rémond, A second gradient continuum model accounting for some effects of micro-structure on reconstructed bone remodelling, C.R. Mec. 340 (8) (2012) 575–589.

[59] W. Pietraszkiewicz, V. Eremeyev, V. Konopińska, Extended non-linear relations of elastic shells undergoing phase transitions, Z. Angew. Math. Mech. 87 (2) (2007) 150–159.

[60] I. Giorgio, A. Culla, D. Del Vescovo, Multimode vibration control using several piezoelectric transducers shunted with a multiterminal network, Arch. Appl. Mech. 79 (9) (2009) 859–879.
[61] U. Andreaus, I. Giorgio, A. Madeo, Modeling of the interaction between bone tissue and resorbable biomaterial as linear elastic materials with voids, Z. Angew. Math. Phys. 66 (1) (2015) 209–237.
[62] R.C. Batra, F. dell'Isola, R.G.C, Second-order solution of Saint-Venant's problem for an elastic bar predeformed in flexure, Int. J. Non Linear Mech. 40 (2) (2005) 411–422.
[63] F. dell'Isola, R.C. Batra, Saint-Venant's problem for porous linear elastic materials, J. Elast. 47 (1) (1997) 73–81.
[64] H. Altenbach, V.A. Eremeyev, N.F. Morozov, Surface viscoelasticity and effective properties of thin-walled structures at the nanoscale, Int. J. Eng. Sci. 59 (2012) 83–89.
[65] J. Beyrouthy, Réduction 3D-1D d'un modèle viscoélastique en grandes déformations, C.R. Math. 345 (4) (2007) 239–243.
[66] A. De Simone, A. Luongo, Nonlinear viscoelastic analysis of a cylindrical balloon squeezed between two rigid moving plates, Int. J. Solids Struct. 50 (14) (2013) 2213–2223.
[67] A.D. Brailsford, The role of internal stresses in internal friction, Phys. Lett. 12 (2) (1964) 92–93.
[68] G. Fantozzi, I.G. Ritchie, Internal friction caused by the intrinsic properties of dislocations, J. Phys. Colloq. 42 (C5) (1981) C5–3.
[69] G. Fantozzi, C. Esnouf, W. Benoit, I.G. Ritchie, Internal friction and microdeformation due to the intrinsic properties of dislocations: The Bordoni relaxation, Prog. Mater. Sci. 27 (3) (1982) 311–451.
[70] A.L. Kimball, D.E. Lovell, Internal friction in solids, Phys. Rev. 30 (6) (1927) 948
[71] C-H. Lamarque, F. Bernardin, J. Bastien, Study of a rheological model with a friction term and a cubic term: deterministic and stochastic cases, Eur. J. Mech. A. Solids 24 (4) (2005) 572–592.
[72] J.C. Savage, J.D. Byerlee, D.A. Lockner, Is internal friction friction?, Geophys. Res. Lett. 23 (5) (1996) 487–490.
[73] C.J. Spears, P. Feltham, On the amplitude-independent internal friction in crystalline solids, J. Mater. Sci. 7 (8) (1972) 969–971.
[74] C. Zener, Internal friction in solids, Proc. Phys. Soc. 52 (1) (1940) 152.
[75] M. Volpato, Sull'esistenza di soluzioni periodiche per equazioni differenziali ordinarie del secondo ordine, Rendiconti del Seminario Matematico della Università di Padova, 25. 1956, 371–385.
[76] A. Cazzani, M. Malagù, E. Turco, Isogeometric analysis of plane-curved beams, Math. Mech. Solids (2014) http://dx.doi.org/10.1177/1081286514531265.
[77] E. Turco, P. Caracciolo, Elasto-plastic analysis of Kirchhoff plates by high simplicity finite elements, Comput. Methods Appl. Mech. Eng. 190 (5) (2000) 691–706.
[78] L. Greco, M. Cuomo, An implicit G1 multi patch B-spline interpolation for Kirchhoff-Love space rod, Comput. Methods Appl. Mech. Eng. 269 (2014) 173–197.
[79] L. Greco, M. Cuomo, B-Spline interpolation of Kirchhoff–Love space rods, Comput. Methods Appl. Mech. Eng. 256 (2013) 251–269.
[80] L. Greco, M. Cuomo, Consistent tangent operator for an exact Kirchhoff rod model, Contin. Mech. Thermodyn. 27 (4) (2015) 861–877.
[81] U. Andreaus, F. dell'Isola, On thermokinematic analysis of pipe shaping in cast ingots: a numerical simulation via FDM, Int. J. Eng. Sci. 34 (12) (1996) 1349–1367.
[82] A. Di Egidio, A. Luongo, A. Paolone, Linear and non-linear interactions between static and dynamic bifurcations of damped planar beams, Int. J. Non Linear Mech. 42 (1) (2007) 88–98.
[83] A. Luongo, D. Zulli, G. Piccardo, On the effect of twist angle on nonlinear galloping of suspended cables, Comput. Struct. 87 (15) (2009) 1003–1014.
[84] V.A. Eremeev, A.B. Freidin, L.L. Sharipova, Nonuniqueness and stability in problems of equilibrium of elastic two-phase bodies, Dokl. Phys. 48 (7) (2003) 359–363.
[85] M. Jamal, L. Lahlou, M. Midani, H. Zahrouni, A. Limam, N. Damil, M. Potier-Ferry, A semi-analytical buckling analysis of imperfect cylindrical shells under axial compression, Int. J. Solids Struct. 40 (5) (2003) 1311–1327.
[86] G. Michel, A. Limam, J.F. Jullien, Buckling of cylindrical shells under static and dynamic shear loading, Eng. Struct. 22 (5) (2000) 535–543.
[87] A. Carcaterra, D. Dessi, F. Mastroddi, Hydrofoil vibration induced by a random flow: a stochastic perturbation approach, J. Sound Vib. 283 (1) (2005) 401–432.
[88] A. Madeo, Effect of Micro-particle Additions on Frictional Energy Dissipation and Strength of Concrete, Virginia Polytechnic Institute and State University 2006. Master's thesis.
[89] F.S. Opie, Jr, C.L. Hulsbos, Probable fatigue life of plain concrete with stress gradient, ACI Proceedings, Vol. 63, Nc. 1, January 1966, Publication No. 295, Fritz Laboratory Reports, 1966.
[90] N.E. Dowling, Mechanical Behavior of Materials, Pearson 2012.
[91] D. Scerrato, Effect of Micro-Particle Addition on Frictional Energy Dissipation and Strength of Concrete: Experiments and Modelling, Theoretical and Applied Mechanics and Mécanique, Énergétique, Génie Civil, Acoustique, 2014. Ph.D. thesis.
[92] H. Aminpour, N.L. Rizzi, A one-dimensional continuum with microstructure for single-wall carbon nanotubes bifurcation analysis, Math. Mech. Solids 21 (2) (2016) 168–181.
[93] N.L. Rizzi, V. Varano, S. Gabriele, Initial postbuckling behavior of thin-walled frames under mode interaction, Thin-Walled Struct. 68 (2013) 124–134.